PNAS RESEARCH ARTICLE | GENETICS OPEN ACCESS

An intraflagellar transport dependent negative feedback regulates the MAPKKK DLK-1 to protect cilia from degeneration

Yue Sun[a] and Yishi Jin[a,1]

Contributed by Yishi Jin; received February 20, 2023; accepted August 15, 2023; reviewed by Maxwell G. Heiman and X.Z. Shawn Xu

Primary cilia are specialized organelles supporting the development and function of cells and organisms. Intraflagellar transport (IFT) is essential for cilia formation, maintenance, and function. In *C. elegans* ciliated sensory neurons, IFT interacts with signaling molecules to generate distinct morphological and function features and also to maintain the integrity of cilia. Here, we report an IFT-dependent feedback control on the conserved MAPKKK DLK-1 in the ciliated sensory neurons. DLK proteins are widely known to act in synapse formation, axon regeneration, and degeneration, but their roles in other neuronal compartments are understudied. By forward genetic screening for altered expression of the endogenously tagged DLK-1 we identified multiple *ift* mutants showing increased DLK-1 accumulation in the defective sensory endings. We show that in response to acute IFT disruption, DLK-1 accumulates rapidly and reversibly. The expression levels of the transcription factor CEBP-1, known to act downstream of DLK-1 in the development and maintenance of synapses and axons, are also increased in the ciliated sensory neurons of *ift* mutants. Interestingly, the regulation of CEBP-1 expression shows sensory neuron-type dependency on DLK-1. Moreover, in the sensory neuron AWC, which has elaborate cilia morphology, up-regulated CEBP-1 represses DLK-1 at the transcription level, thereby dampening DLK-1 accumulation. Last, the IFT-dependent regulatory loop of DLK-1 and CEBP-1 offers neuroprotection in a cilia degeneration model. These findings uncover a surveillance mechanism in which tight control on the DLK-1 signaling protects cilia integrity in a context-specific manner.

cilia degeneration | AWC sensory neuron | CHE-3 dynein | CHE-10 Rootletin | CEBP-1 bZIP protein

Significance

Neurons require compartmentalized actions of molecules to sustain function under various stress conditions. The conserved MAPKKK DLKs are key stress-sensing kinases extensively studied for their roles in synapses and axons. However, their function in other neuronal compartments is not well explored. Here, we identified a mechanism by which intraflagellar transport (IFT) actively represses accumulation of *C. elegans* DLK-1 in the ciliated sensory neurons. Disruption in IFT activates DLK-1 and increases expression of its downstream transcription factor CEBP-1, which in turn represses *dlk-1* transcription. This IFT-dependent negative feedback regulation of DLK-1 offers protective roles in cilia undergoing degeneration. Our findings uncovered a homeostatic mechanism regulating DLK-1 signaling in sensory neurons.

Cilia are microtubule-based organelles present in many types of cells. Nonmotile primary cilia projecting from the cell surface detect environmental stimuli and trigger cellular responses to prompt proper actions of cells or organisms. Cilia formation and maintenance require exquisite regulation from gene expression to intracellular trafficking and membrane remodeling (1, 2). A key transport machinery in cilia is the intraflagellar transport (IFT), which utilizes the anterograde motor kinesin-2 and retrograde motor dynein-2 to deliver cargoes bidirectionally between the base and the distal tip of a cilium (3–5). In most cilia, IFT function requires two multisubunit protein complexes, known as IFT-A and IFT-B, that coordinate the interaction between the motors and cargoes (6–8). A long-standing interest has been to understand how IFT regulates cilia proteome to ensure morphological integrity and functional diversity of cilia (4, 6, 9).

The nematode *Caenorhabditis elegans* has a rich set of sensory neurons that rely on cilia to detect specific stimuli and to regulate neuronal circuits and animal behaviors (9, 10). Extensive studies have revealed many conserved mechanisms in cilia formation and function. For example, the RFX transcription factor DAF-19 regulates ciliary gene expression and is required for cilia formation of all sensory neurons (11, 12). Rootletin/CHE-10 anchors cilium to basal bodies and facilitates IFT assembly in multiple types of sensory neurons (13, 14). Different IFT-A and IFT-B components function cooperatively in cilia formation and maintenance to endow cell-type specificity among sensory neurons (15). Additionally, a wide range of signaling molecules interact with IFT to generate cilia- and neuron-type specificity. For example, the conserved kinase MAK/DYF-5 interacts with IFT and microtubules to regulate cilia length and arborization (16–18). Differential expression levels of an immunoglobulin (Ig)-domain protein OIG-8 help to establish cilia morphological diversity (19). Emerging findings have continuously expanded the complex landscape of cilia proteins and their signaling network.

We are interested in the regulation of the *C. elegans* DLK-1, a member of the conserved MAPKKK Dual Leucine zipper-bearing Kinases (DLKs) that include vertebrate DLK/MAP3K12 and LZK/MAP3K13, and *Drosophila* DLK/Wallenda. The functions of these MAPKKKs have been widely studied in synapse formation, axon regeneration and degeneration, and neuronal survival (20). Multiple factors are known to regulate the activity of DLKs in these contexts, such as the E3 ubiquitin ligase PHR proteins (21–23), the

Author affiliations: [a]Department of Neurobiology, School of Biological Sciences, University of California San Diego, La Jolla, CA 92093

Author contributions: Y.S. and Y.J. designed research; Y.S. performed research; Y.S. and Y.J. analyzed data; and Y.S. and Y.J. wrote the paper.

Reviewers: M.G.H., Harvard Medical School; and X.Z.S.X., University of Michigan, Ann Arbor.

The authors declare no competing interest.

[1]To whom correspondence may be addressed. Email: yijin@ucsd.edu.

This article contains supporting information online at https://www.pnas.org/lookup/suppl/doi:10.1073/pnas.2302801120/-/DCSupplemental.

chaperones Hsp70 and Hsp90 (24–26), protein palmitoylation (27, 28), and calcium and cAMP signalings (29–31). In contrast, few studies have addressed the function and regulation of DLKs in other compartments of neurons. In mature hippocampal neurons, DLK is present in postsynaptic density and may regulate dendritic spine size and synaptic strength (32). In *C. elegans,* hyperactivation of a Gα protein in several amphid sensory neurons shortens the cilia length through DLK-1 and its downstream p38 MAP kinase, partly via regulating RAB-5 mediated endocytosis (33). Endosomal regulation by DLK-1 is also shown to selectively stabilize the photoreceptor LITE-1 in the polymodal sensory neuron ASH, albeit independent of cilia (34). Nonetheless, it remains poorly understood of how DLK-1 is regulated in compartmentalized space of neurons.

Here, by genetic screening for additional regulators of DLK-1, we find that IFT actively represses DLK-1 expression in the ciliated sensory neurons. Upon acute IFT disruption, DLK-1 accumulates in the sensory endings rapidly and reversibly. The increased accumulation of DLK-1 in *ift* mutants is accompanied by an upregulation of the bZIP transcription factor CEBP-1, previously known to act downstream of the DLK-1 kinase cascade. Interestingly, the upregulation of CEBP-1 in the ciliated sensory neurons shows cell-type dependency on DLK-1. Furthermore, in the AWC neurons, which have elaborate cilia morphology, CEBP-1 represses *dlk-1* transcription in a manner dependent on IFT. Last, we show that the IFT-dependent DLK-1 to CEBP-1 signaling has a neuroprotective role in a cilia degeneration model.

Results

Loss-of-Function Mutations in Multiple *ift* Genes Cause Accumulation of GFP::DLK-1 in the Sensory Endings of Ciliated Neurons. In previous studies that characterized the function of DLK-1 in synapses and axons, the expression of DLK-1 was observed primarily using transgenic reporters that overexpressed DLK-1 tagged with fluorescent proteins under neuron-specific promoters (23, 26, 29, 31, 33, 35). Here, we aimed to examine endogenous DLK-1 protein expression by inserting Green Fluorescent Protein (GFP) at the N terminus of DLK-1 through CRISPR-Cas9 genome editing [*SI Appendix*, Fig. S1*A* and *Materials and Methods*; allele designated as *GFP::dlk-1(ju1579)*]. We confirmed the production of *GFP::dlk-1* mRNA by RT-PCR analysis (*SI Appendix*, Fig. S1*B*). However, GFP fluorescence was very weak for visible detection in any tissue at any stage of animals (Fig. 1*A* and *SI Appendix*, Fig. S1*C*), in line with the general observation that DLK-1 is normally kept at low levels. In the E3 ligase *rpm-1(0)* mutants, increased GFP::DLK-1 expression was detected in the nervous system (*SI Appendix*, Fig. S1*C*), with about threefold increase of the fluorescence intensity in the nerve ring, compared to the control (*SI Appendix*, Fig. S1*D*). Homozygous *GFP::dlk-1(ju1579)* animals showed normal fertility, locomotion, and growth rate. The axon morphology of touch receptor neurons and synapses of the GABAergic motor neurons were grossly normal (*SI Appendix*, Fig. S1 *E–H*). Loss of *dlk-1* suppresses synapse and axon defects in *rpm-1(0)* and impairs axon regeneration following laser axotomy (23, 36, 37). We found that synapse and axon morphology in *GFP::dlk-1(ju1579); rpm-1(0)* animals were indistinguishable from *rpm-1(0)* (*SI Appendix*, Fig. S1 *E–H*); *GFP::dlk-1(ju1579)* animals showed normal axon regeneration (*SI Appendix*, Fig. S2*C*). These data support the conclusion that *GFP::dlk-1(ju1579)* retains the normal function of *dlk-1*.

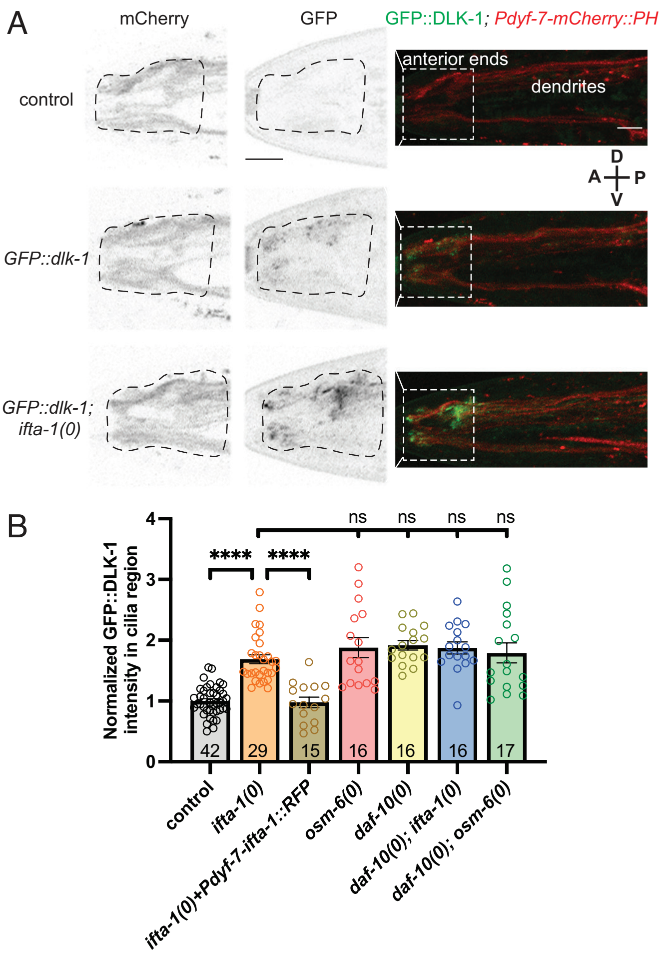

Fig. 1. Endogenous DLK-1 accumulates in the sensory endings of *ift* mutants. (*A*) Confocal Z-stack projection images of anterior ends in L2 animals of indicated genotypes, with the same orientation along the body axis (A, anterior; P, posterior; D, dorsal; V, ventral). Allele designation is *GFP::dlk-1(ju1579), ifta-1(ju1644), Pdyf-7-mCherry::PH(ltSi1033).* Dashed boxes in the right panels mark the anterior ends of ciliated neurons, including cilia and distal dendrites. Dashed areas in the left and middle panels outline the region of interest (ROI) for fluorescence intensity quantification. (Scale bars: 5 μm.) (*B*) Quantification of GFP::DLK-1 fluorescence intensity in L4 animals. Data are represented as mean ± SEM; each circle represents an individual animal with fluorescence value normalized to the average value of control animals from the same experiment. Null *(0)* alleles are *ifta-1(ju1644), osm-6(sa119),* and *daf-10(gk795).* The total number of animals per genotype collected from two to three experiments is shown in the columns. Statistics: Welch's ANOVA test with multiple comparison, corrected with the FDR method of Benjamini and Hochberg. ns, $P > 0.05$. ****$P < 0.0001$.

We then conducted a forward genetic screen to search for mutants that showed altered expression of GFP::DLK-1 (*Materials and Methods*). We found multiple mutants showing increased GFP::DLK-1 at the anterior ends of the animals. Using a pan-ciliated neuron membrane marker *Pdyf-7-mCherry::PH(ltSi1033)* (38), we confirmed that the area with increased GFP::DLK-1 corresponded to the region containing most sensory endings (Fig. 1*A*). By a combination of whole-genome sequencing (WGS) analysis and genetic mapping (*Materials and Methods*), we identified mutagenesis-induced nucleotide changes in several *ift* genes, including *ifta-1/IFT121* and *daf-10/IFT122,* encoding IFT-A proteins (39, 40) and *che-3,* encoding the dynein-2 heavy chain DYNC2H1 (41) (*SI Appendix*, Table S2). By outcrossing and noncomplementation test, we verified that these mutations caused loss of function in the respective *ift* genes (*Materials and Methods*). We also examined previously reported loss-of-function mutations in these *ift* genes and observed similar accumulation of GFP::DLK-1 in the sensory endings (*SI Appendix*, Table S2).

Two studies have reported the roles of DLK-1 in amphid sensory neurons ASI and ASH (33, 34). However, the low expression and diffused cytoplasmic localization of DLK-1 precluded the identification of how many ciliated sensory neurons express DLK-1. In our genetic screen, we isolated a mutant that displayed increased GFP::DLK-1 in the somatic cytoplasm of many neurons (*SI Appendix*, Fig. S2*A*). We mapped this mutation, *ju1626,* to a single nucleotide alteration in exon 6 of *dlk-1,* changing the conserved Pro366 to Leu within the kinase domain (*SI Appendix*, Fig. S2*B* and Table S2). We further engineered the same nucleotide change *(ju1992)* in *GFP::dlk-1(ju1579)* animals by CRISPR-Cas9 genome editing and observed soma-enriched fluorescence of GFP::DLK-1 indistinguishable from *ju1626*. Pro366 resides in the C-lobe of the DLK-1 kinase domain; the C-lobe in several kinases can interact with chaperone Hsp90 (42). It is possible that P366L substitution may alter folding of DLK-1 protein and trap the mutant protein in somatic compartments for protein processing. *dlk-1(P366L)* behaved as a genetic null mutation since it fully suppressed the touch receptor neuron axon termination defects of *rpm-1(0)* and also failed to regenerate axons after laser injury (*SI Appendix*, Fig. S2 *C* and *D*). As the single nucleotide alteration in *dlk-1(P366L)* is unlikely to alter the transcription or mRNA processing of *dlk-1,* we took advantage of the soma-enriched fluorescence of GFP::DLK-1(P366L) to identify cells that express DLK-1. Using a pan-ciliated neuron nuclei marker *Pdyf-7-mCherry::his-72(ltSi1050)* (38), we observed that GFP::DLK-1(P366L) was visible in all ciliated neurons (*SI Appendix*, Fig. S2*E*), and not detectable in non-neuronal cells surrounding the ciliated neurons.

We addressed whether DLK-1 accumulation in *ift* mutants is due to cell-autonomous function of the *ift* genes. We expressed wild-type *ifta-1* cDNA using the *dyf-7* promoter (*Pdyf-7-ifta-1cDNA::tagRFP*) and observed that the accumulation of GFP::DLK-1 in *ifta-1(0)* mutant was fully rescued (Fig. 1*B*). To address whether the *ift* genes affected DLK-1 in the same pathway, we analyzed *daf-10(0); ifta-1(0)* double mutants and found that they showed increased GFP::DLK-1 indistinguishably from each single mutant (Fig. 1*B*). Mutants of *osm-6/IFT52,* an IFT-B protein (39, 43) also showed GFP::DLK-1 accumulation similar to either *daf-10(0)* or *ifta-1(0)*; and *daf-10(0); osm-6(0)* double mutants resembled each single mutant (Fig. 1*B*). These data support a conclusion that disruption of the IFT machinery causes improper accumulation of GFP::DLK-1 in the sensory endings of ciliated neurons. In *rpm-1(0)* mutant GFP::DLK-1 was increased primarily in the nerve ring (*SI Appendix*, Fig. S1 *C* and *D*), whereas the *ift* mutants showed no significantly altered DLK-1 expression in the nerve ring or axons of ciliated neurons (Fig. 1*A* and *SI Appendix*, Fig. S1*C*). These observations suggest that DLK-1 expression in ciliated sensory neurons is likely regulated by a distinct mechanism.

DLK-1 in Cilia Does Not Resemble IFT Particles. In neuronal axons, DLK-1 and its homologs are known to be associated with transporting vesicles (27, 44, 45). We thus asked whether DLK-1 could be associated with IFT in ciliated sensory neurons. The nearly invisible GFP::DLK-1*(ju1579)* fluorescence was incompatible for colocalization analysis with IFT markers; we therefore examined a transgene *juIs192* that expresses DLK-1::GFP under the *dlk-1* promotor and does not alter axon and synapse architecture (23). *juIs192[DLK-1::GFP]* animals showed no difference from wild-type animals in the lipophilic dye DiI (1,1′-dioctadecyl-3,3,3′,3′,-tetramethylindocarbocyanine perchlorate) uptake assay (*SI Appendix*, Table S3), suggesting that most cilia are normal. In ciliated neurons, DLK-1::GFP displayed diffuse and punctate patterns (Fig. 2*A*). We analyzed colocalization of DLK-1::GFP with XBX-1::tagRFP(*cas502*), representing the dynein light intermediate chain of IFT (46, 47). By confocal imaging analysis, we detected some DLK-1::GFP puncta to be close to, or partly overlapping with, XBX-1::tagRFP puncta in cilia (insets in Fig. 2*A*). As a control, XBX-1::tagRFP showed a complete colocalization with the dynein heavy chain of IFT CHE-3::GFP (*cas443*). In *ifta-1(0)* mutants in which many cilia are shortened (40), DLK-1::GFP fluorescence was increased in the remaining sensory endings, with the pattern remained as diffuse and punctate, while XBX-1::tagRFP showed strong accumulation at the amphid cilia base, greatly reduced number of puncta in the remaining cilia, and also cosegregated with CHE-3::GFP (Fig. 2*A*). We observed a similar spatial pattern of DLK-1::GFP with an IFT-B component OSM-6::mCherry(*casIs550*). In *ifta-1(0)*, colocalization analysis of GFP::DLK-1*(ju1579)* with a cilia marker (*Pdyf-7-arl-13cDNA::tagRFP*) and a periciliary membrane compartment (PCMC) marker (*Pdyf-7-tram-1cDNA::tagRFP*) showed that some GFP::DLK-1 puncta overlapped with ARL-13 labeled cilia stumps (*SI Appendix*, Fig. S2*G*) and that GFP::DLK-1 was also present in the distal dendrites posterior to PCMC (*SI Appendix*, Fig. S2*F*). We attempted to assess the localization of GFP::DLK-1(*ju1579*) in a single cilium by examining the amphid neuron

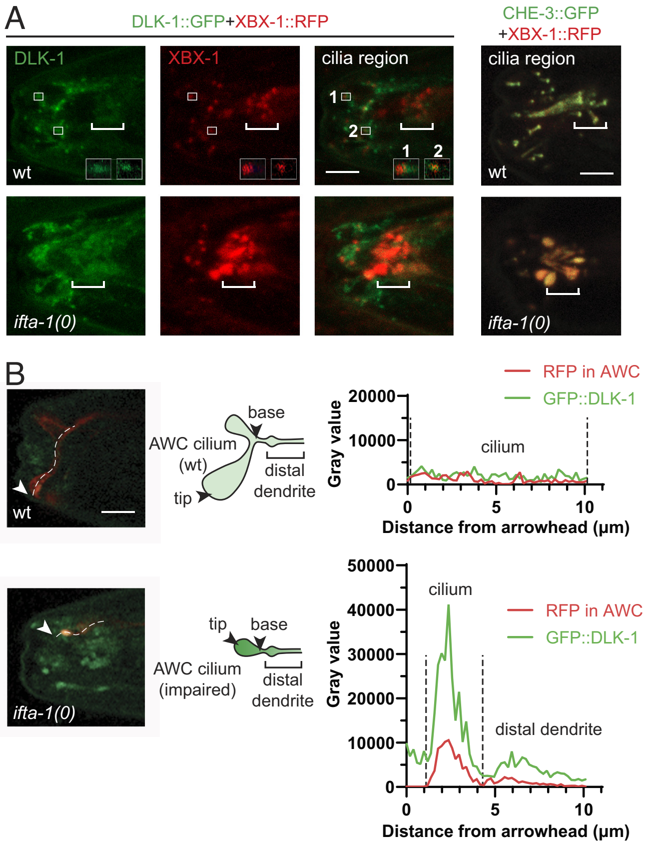

Fig. 2. DLK-1 is not tightly associated with IFT particles. (*A*) Shown are confocal Z-stack images of coexpression of DLK-1::GFP(*juIs192*) with the dynein-2 light intermediate chain XBX-1::tagRFP(*cas502*) in the cilia region. The *Insets* in wild type (wt) show enlarged single-plane images where punctate DLK-1::GFP are seen adjacent to or partly overlap with XBX-1::tagRFP puncta. In *ifta-1(0)* animals, XBX-1::tagRFP is predominantly seen in the amphid cilia base, while DLK-1::GFP intensity increases and remains diffuse and punctate. Right column of images show the dynein heavy chain CHE-3::GFP(*cas443*) colocalizes with XBX-1::tagRFP in wild-type animals and cosegregates in *ifta-1(0)* animals. White brackets indicate the amphid cilia base. (Scale bar: 5 μm.) (*B*) Plot profile analysis of GFP::DLK-1(*ju1579*) in AWC marked by *Podr-1-RFP(oyIs44)* shows that in wild-type AWC cilia wing has no or very low GFP::DLK-1 and in *ifta-1(0)* animals GFP::DLK-1 accumulates in cilia stump and distal dendrites. Left panels are confocal images of AWC, along with illustration. Line profiles correspond to the dashed lines in AWC images, and white arrowheads mark AWC cilia tips indicated by RFP. (Scale bar: 5 μm.)

AWC labeled with *Podr-1-RFP(oyIs44)* (48). In wild-type animals, AWC cilia showed two fan-shaped wings, and GFP::DLK-1 was largely invisible in cilia wing (Fig. 2*B*). In *ifta-1(0)* animals, the fan-shaped cilia of AWC were reduced to a knob, GFP::DLK-1 was accumulated in the remaining cilia stump and distal dendrites of AWC (Fig. 2*B*). These data show that DLK-1 is unlikely a component of IFT particles. However, it remains to be addressed whether endogenously expressed DLK-1 localizes to any subcellular compartments of the sensory endings.

DLK-1 Accumulates Rapidly and Reversibly upon Acute IFT Disruption. In *ift* mutants, both cargo transport and cilia morphology are disrupted. We wondered whether simply altering cilia morphology could affect DLK-1. Loss of function in the Ig-domain protein OIG-8 or ciliary β-tubulin TBB-4 alters cilia morphology and reduces cilia size in multiple sensory neurons and does not alter IFT (19, 49, 50). We did not observe GFP::DLK-1 accumulation in the cilia of *oig-8(0)* and *tbb-4(0)* mutants (*SI Appendix*, Fig. S3*A*). Loss of function in the MAK kinase *dyf-5* alters IFT and causes more or ectopic growth of cilia (16). We observed GFP::DLK-1 accumulation in the cilia of *dyf-5(0)* (*SI Appendix*, Fig. S3*A*). These observations suggest that accumulation of GFP::DLK-1 in *ift* mutants does not simply result from altered cilia volume and hint at a strong connection between IFT and DLK-1 abundance in cilia.

We next addressed whether DLK-1 accumulation in cilia is an active response to IFT disruption by examining *che-3(nx159ts)*, a temperature-sensitive mutant caused by a Gly1997Glu missense mutation in the second AAA ATPase domain of the dynein-2 heavy chain protein (41, 51). At permissive temperature (15 °C), cilia of *che-3(nx159ts)* show normal anterograde IFT and moderately reduced retrograde transport. At nonpermissive temperature (25 °C), cilia of *che-3(nx159ts)* display no transport, with IFT components trapped at the cilia base. Within 3 h of upshifting from 15 °C to 25 °C, *che-3(nx159ts)* shows altered IFT dynamics in both directions (51).

We first verified temperature-sensitive effects of *che-3(nx159ts)* on an IFT-B component IFT-74::GFP(*cas499*) (46) and GFP::DLK-1. In control (wild-type) animals maintained at either 15 °C or 25 °C, IFT-74::GFP particles were present along the cilia, with moderate enrichment at the amphid cilia base (Fig. 3 *A*–*C*). The pattern of IFT-74::GFP in *ifta-1(0)* also did not show any temperature dependency (Fig. 3*C*). In *che-3(nx159ts)* animals maintained at 15 °C, patterns of IFT-74::GFP particles along the cilia resembled those in control, but the fluorescence intensity at the amphid cilia base was increased by about twofold. In *che-3(nx159ts)* animals maintained at 25 °C or upshifted from 15 °C to 25 °C for 24 h, IFT-74::GFP accumulation at the amphid cilia base was further increased, with very few particles detectable at the remaining cilia (Fig. 3 *A*–*C*). The fluorescence intensity of GFP::DLK-1 in the cilia region of *che-3(nx159ts)* animals maintained at 15 °C was higher than that in control (Fig. 3 *D* and *E*). In *che-3(nx159ts)* animals maintained at 25 °C or upshifted from 15 °C to 25 °C for 24 h, GFP::DLK-1 intensity was increased to the same level as in *ifta-1(0)* animals. We also examined the temperature effects of *che-3(nx159ts)* on AWC cilia morphology. In *che-3(nx159ts)* maintained at 15 °C, AWC developed single fan-shaped cilia or two cilia branches without fan shape, and the total cilia area was reduced to about 50% of that in wild type. In *che-3(nx159ts)* maintained at 25 °C, the AWC cilia displayed a knob shape (*SI Appendix*, Fig. S3 *B* and *C*).

We then tested the effects of acute disruption of IFT by upshifting *che-3(nx159ts)* and control animals from 15 °C to 25 °C for 3 h. In control and *che-3(nx159ts)* animals, we did not detect significant changes in IFT-74::GFP pattern and fluorescence intensity (Fig. 3 *B* and *C*), or in AWC cilia morphology (*SI Appendix*, Fig. S3 *B* and *C*). In contrast, we observed that upon upshifting from 15 °C to 25 °C for 3 h, the fluorescence intensity of GFP::DLK-1 in the cilia region of *che-3(nx159ts)* animals was significantly increased to the level comparable to that in *ifta-1(0)* animals and did not further increase when maintained at 25 °C for longer (Fig. 3 *D* and *E*). This result shows that GFP::DLK-1 responds rapidly to acute IFT disruption, preceding detectable changes of IFT-74::GFP and AWC cilia morphology. We next addressed whether the *che-3*-dependent accumulation of GFP::DLK-1 was reversible. We subjected *che-3(nx159ts)* animals to upshifting from 15 °C to 25 °C for 3 h followed by downshifting to 15 °C for 3 h (Fig. 3*A*) and observed GFP::DLK-1 accumulation in the cilia region resembled that in *che-3(nx159ts)* maintained at 15 °C (Fig. 3 *D* and *E*). This analysis implies that the *che-3*-induced DLK-1 accumulation following 3 h of upshifting can be reversed.

We further addressed whether IFT-induced GFP::DLK-1 accumulation might depend on the functionality of DLK-1. We performed the same temperature shift analysis on the nonfunctional GFP::DLK-1(P366L). *che-3(nx159ts) GFP::dlk-1(P366L)* animals cultured at 15 °C showed GFP::DLK-1(P366L) accumulation in the cilia region similar to *GFP::dlk-1(P366L)* alone. Upon upshifting from 15 °C to 25 °C for 3 h, GFP::DLK-1(P366L) accumulation in *che-3(nx159ts) GFP::dlk-1(ju1626)* increased significantly, but to a lesser degree than that of GFP::DLK-1 in *che-3(nx159ts)*. Different from GFP::DLK-1, GFP::DLK-1(P366L) continued to accumulate when kept at 25 °C for longer. Moreover, under the scheme of upshifting for 3 h followed by downshifting for 3 h, GFP::DLK-1(P366L) remained high (Fig. 3 *A*, *D*, and *F*). This analysis suggests that the protein activity of DLK-1 is necessary for the rapid and reversible accumulation of DLK-1 in response to acute IFT disruption.

CEBP-1 Expression Is Elevated in Ciliated Neurons of *ift* Mutants and Shows Neuron-Type Dependency on *dlk-1*. Increased expression of DLK-1 is known to activate the downstream MAP kinase signal transduction (23, 37). A key downstream target of DLK-1 signaling pathway is the bZIP transcription factor CEBP-1 (37, 52). We next asked whether the increased accumulation of DLK-1 in the sensory endings of *ift* mutants would result in activation of its downstream signaling. We visualized CEBP-1 expression using a fosmid reporter *wgIs563[cebp-1::GFP]* or a knock-in reporter *cebp-1::GFP(st12290)*. In wild-type animals, CEBP-1::GFP was detected in all somatic nuclei. In *rpm-1(0)* animals, CEBP-1::GFP intensity was increased in many neurons in the ventral nerve cord, head and tail ganglia (*SI Appendix*, Fig. S4 *A* and *B*), consistent with previous findings (37). In *ifta-1(0)* single or *daf-10(0); osm-6(0)* double mutants, CEBP-1::GFP intensity was selectively increased in the ciliated neurons marked by *Pdyf-7-mCherry::his-72* (Fig. 4 *A* and *B* and *SI Appendix*, Fig. S4*A*). As a control for the selectivity of CEBP-1 upregulation in response to IFT disruption, we examined the cilia-specific RFX transcription factor DAF-19 (11, 12), which has no known interactions with DLK-1. The intensity of DAF-19::GFP in *ifta-1(0)* animals remained similar to that in wild type (*SI Appendix*, Fig. S4*C*). Additionally, in *oig-8(0)* or *tbb-4(0)* mutants, which did not show increased accumulation of GFP::DLK-1 in cilia, CEBP-1::GFP intensity remained the same as in wild type. In contrast, in *dyf-5(0)* mutants, CEBP-1::GFP intensity was increased in the sensory neurons, albeit to a lesser degree than in *ift* mutants (*SI Appendix*, Fig. S4*D*). These observations indicate that increased DLK-1 accumulation in *ift* mutants results in its activation, leading to increased CEBP-1 expression.

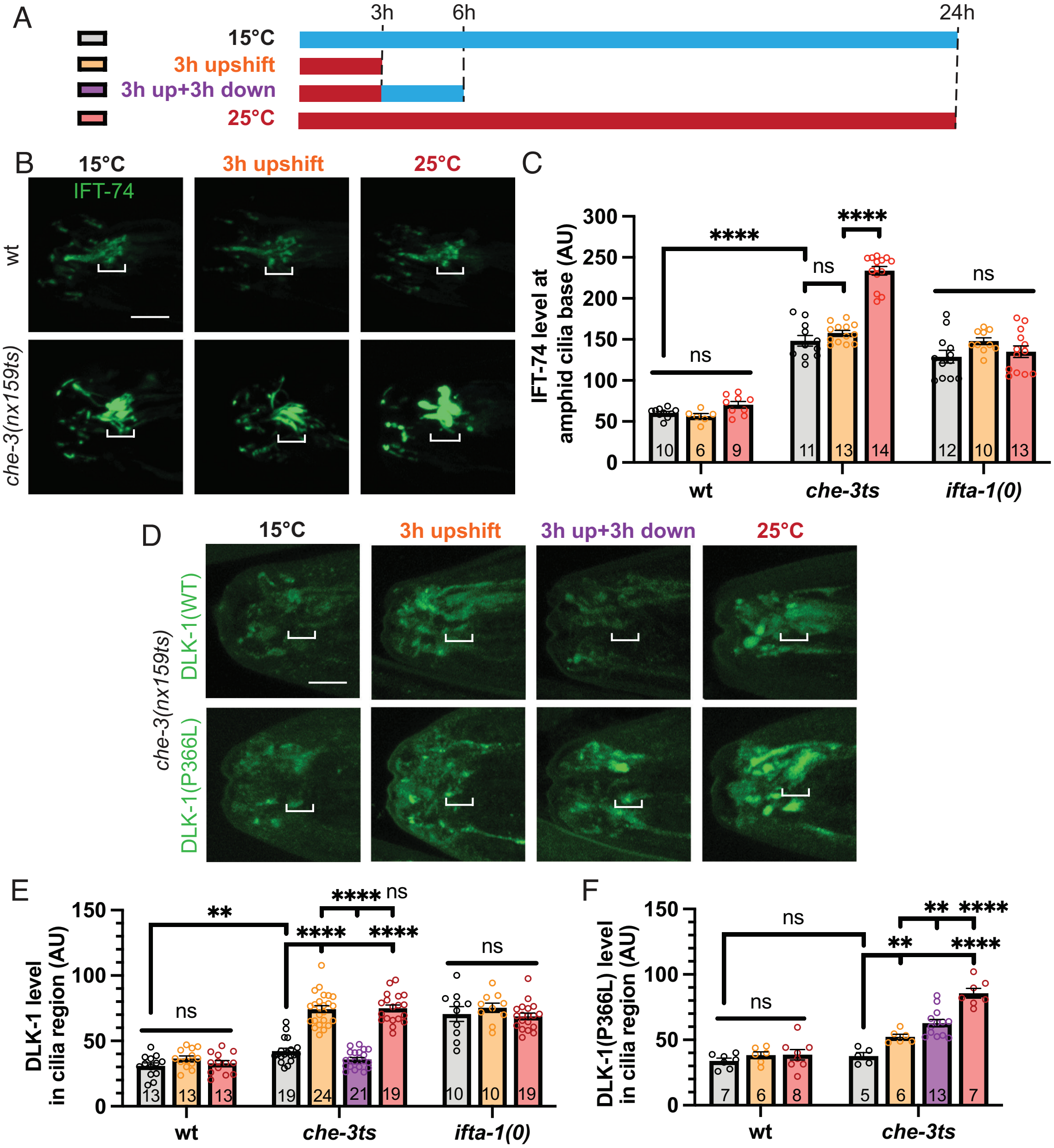

Fig. 3. DLK-1 accumulates reversibly in response to acute disruption of IFT. (*A*) Temperature shift scheme: animals were maintained at 15 °C (blue) and upshifted to 25 °C (red) for hours indicated. L4 animals were collected at the time points marked by vertical dashed lines and imaged within 20 min. Different experimental groups were labeled by colored letters, corresponding to the colored columns in the quantification graphs in *C*, *E*, and *F*. (*B*) Z-stack confocal images of IFT-74::GFP*(cas499)* in the cilia region from wild-type and *che-3(nx159ts)* animals at different temperature conditions as indicated. White brackets mark the region corresponding to the amphid cilia base. (Scale bar: 5 μm.) (*C*) Quantification of IFT-74::GFP intensity in the amphid cilia base under indicated temperature conditions shown in *A*. Data are represented as mean ± SEM, with each circle representing an individual animal and total number of animals analyzed shown in the columns. Statistics: Welch's ANOVA test with multiple comparison, corrected with the FDR method of Benjamini and Hochberg. ns, $P > 0.05$. ****=$P < 0.0001$. (*D*) Z-stack confocal images of GFP::DLK-1(WT) and GFP::DLK-1(P366L) in the cilia region of *che-3(nx159ts)* animals at temperature conditions as indicated. White brackets mark the region corresponding to the amphid cilia base. (Scale bar: 5 μm.) (*E* and *F*) Quantification of GFP::DLK-1 (*E*) and GFP::DLK-1(P366L) (*F*) intensity in the cilia region under indicated temperature conditions shown in *A*. Data are represented as mean ± SEM, with each circle representing an individual animal and total numbers of animals analyzed shown in the columns. Statistics: Welch's ANOVA test with multiple comparison, corrected with the FDR method of Benjamini and Hochberg. ns, $P > 0.05$. ** = $0.01 > P > 0.001$. ****=$P < 0.0001$.

In synapse and axon development and axon regeneration, CEBP-1 expression is mostly dependent on *dlk-1* (37); for example, the increased expression of CEBP-1::GFP in *rpm-1(0)* was eliminated by *dlk-1(0)* (*SI Appendix*, Fig. S4 *A* and *B*). In contrast, by visual observation, we found that in *dlk-1(0); ifta-1(0)* double mutants, only a fraction of sensory neurons showed reduced CEBP-1::GFP, compared to *ifta-1(0)* (Fig. 4 *A* and *B*), suggesting that CEBP-1 expression in ciliated neurons may have selective dependence on *dlk-1*. To gain clues to the sensory neuron-type specificity, we performed confocal imaging analysis and quantitated CEBP-1::GFP intensity in the wing-cilia neurons AWB and AWC and the rod-cilia neurons ASH and ASI. CEBP-1::GFP intensity in these neurons was significantly increased in *ifta-1(0)*, compared to wild type and *dlk-1(0)* (Fig. 4 *C* and *D*). In *dlk-1(0); ifta-1(0)* animals, the increased CEBP-1::GFP in AWB and AWC was reduced to the level similar to *dlk-1(0)* and wild type. In contrast, the increased CEBP-1::GFP in ASH and ASI of *ifta-1(0)* remained in *dlk-1(0); ifta-1(0)* (Fig. 4 *C* and *D*). These observations show

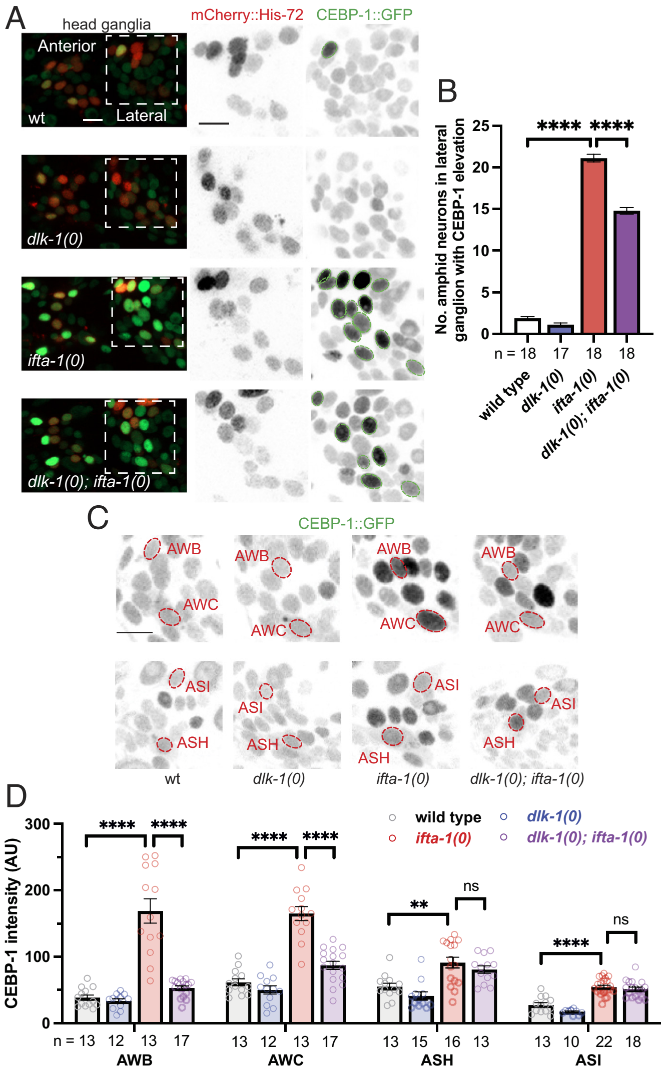

Fig. 4. CEBP-1 expression is increased in ciliated sensory neurons of *ift* mutants, selectively dependent of *dlk-1.* (*A*) Shown are confocal Z-stack images of CEBP-1::GFP*(wgIs563)* in L4 animals of indicated genotypes, with *Pdyf-7-mCherry::his-72(ltSi1050)* marking the nuclei of ciliated neurons. White dashed boxes mark lateral ganglia regions. Green dashed circles mark the nuclei of the ciliated neurons in the lateral ganglia showing increased fluorescence of CEBP-1::GFP compared to the nearby non-neuronal somatic cells in the same animal. Null *(0)* alleles used are *dlk-1(km12), ifta-1(ju1644)*. (Scale bar: 10 µm.) (*B*) Quantification of neurons showing visually detectable increased fluorescence of CEBP-1::GFP compared to the nearby non-neuronal cells under compound fluorescence microscope. Data are represented as mean ± SEM. Numbers of animals analyzed are shown below each column. Statistics: Dunn's multiple comparison test. *****P* < 0.0001. (*C*) Shown are confocal Z-stack images of CEBP-1::GFP in the nuclei of AWB and AWC (marked by red dashed circles based on *Podr-1-RFP*), of ASH and ASI (marked by red dashed circles based on *Psra-6-mcherry*) from L4 animals of indicated genotypes. (Scale bar: 10 µm.) (*D*) Quantification of CEBP-1::GFP fluorescence intensity in AWB, AWC, ASH, and ASI from animals of indicated genotypes. Data are represented as mean ± SEM, with each circle representing an individual animal and total numbers of animals per genotype shown below each column. Statistics: Welch's ANOVA test with multiple comparison, corrected with the FDR method of Benjamini and Hochberg. ns, *P* > 0.05. ** = 0.01 > *P* > 0.001. ****=*P* < 0.0001.

that in AWB and AWC neurons, IFT regulates CEBP-1 expression through DLK-1, whereas in ASH and ASI neurons, IFT regulates CEBP-1 independent of DLK-1. For the rest of analyses, we focused on AWB and AWC to dissect the regulation on DLK-1 and CEBP-1 signaling.

CEBP-1 Represses DLK-1 Expression in the Ciliated Neurons of *ift* Mutant. Since DLK-1 accumulates rapidly following *che-3(nx159ts)*-induced IFT disruption, we next addressed the time course of CEBP-1 upregulation. We measured the fluorescence intensity of CEBP-1::GFP in AWB and AWC of *che-3(nx159ts)* animals following the temperature shift scheme shown in Fig. 3*A*. In *che-3(nx159ts)* cultured at 15 °C, the fluorescence intensity of CEBP-1::GFP in both AWB and AWC was twofold higher than that in wild type. Following upshifting from 15 °C to 25 °C for 3 h, CEBP-1::GFP did not show a significant increase, nor was there any detectable change of CEBP-1::GFP under the scheme of upshifting for 3 h followed by downshifting for 3 h. After 24 h at 25 °C, the CEBP-1::GFP level in both AWB and AWC was significantly increased compared to that at 15 °C. CEBP-1::GFP levels in wild-type animals were comparable, independent of the culture temperature (*SI Appendix*, Fig. S5 *A*–*C*). These observations show that upon IFT disruption, increased CEBP-1 expression follows a slower time course than that of DLK-1 accumulation.

In the course of analyzing compound mutants among *ift*, *cebp-1*, and *dlk-1*, we noticed a synthetic effect such that GFP::DLK-1 intensity in the cilia area or in a single AWC cilium was visibly higher in *cebp-1(0); ift(0)* double mutants than that in *ift(0)* or *cebp-1(0)* single mutants (Fig. 5 *A* and *B*). We did not observe such an effect with the inactive GFP::DLK-1(P366L) (Fig. 5 *C* and *D*), which also blocked the upregulation of CEBP-1::GFP in AWC neurons of *ifta-1(0)*. We thus hypothesized that the elevated expression of CEBP-1 in *ift* mutants may repress DLK-1 expression at the transcription level. To test this, we performed smFISH [single-molecule fluorescence in situ hybridization (53)] analysis on *dlk-1* mRNAs. In L4 animals of wild type, *ifta-1(0)* and *cebp-1(0)*, a few *dlk-1* smFISH signals were detected in the head ganglia. In *cebp-1(0) ifta-1(0)* double mutants, we observed more *dlk-1* smFISH signals distributed broadly in the same area (Fig. 5*E*). We quantitated *dlk-1* smFISH signals in AWC neurons labeled with *Pstr-2-GFP(kyIs140)* (54) and found that AWC neurons in *ifta-1(0) cebp-1(0)* had significantly more *dlk-1* smFISH signals than in wild type, *ifta-1(0)* or *cebp-1(0)* single mutants (Fig. 5 *E* and *F*). This analysis supports a conclusion that increased expression of CEBP- 1 following IFT disruption acts in a negative feedback manner to down-regulate *dlk-1* expression.

Degeneration of Wing Cilia Correlates with Increased DLK-1 and CEBP-1. We next addressed the functional impact of the IFT-dependent regulation of DLK-1 and CEBP-1. Loss of function or overexpression of *dlk-1* or *cebp-1* did not alter animals' ability to uptake the lipophilic dye DiI (*SI Appendix*, Table S3), suggesting that cilia of many sensory neurons are grossly normal. AWC and AWB cilia morphology defects in *ifta-1(0)* mutants were not altered by loss of *dlk-1* or *cebp-1* (Fig. 5 *A* and *D*). However, in the course of analyzing *che-3(nx159ts)* following upshifting to 25 °C for different hours, we noticed that loss of *cebp-1* accelerated AWC cilia morphology deterioration. For example, following upshifting from 15 °C to 25 °C for 6 h, AWC cilia in *che-3(nx159ts)* animals showed single fan-shaped wing or two branches, similar to *che-3(nx159ts)* animals cultured at 15 °C. In *che-3(nx159ts); cebp-1(0)* double mutants, AWC cilia displayed a knob shape in 25% of animals under the same condition (*SI Appendix*, Fig. S5*D*). The observed AWC cilia morphology deterioration is reminiscent of the reported cilia shortening or degeneration in *che-3(nx159ts)* following temperature upshifting (51), suggesting that the IFT-dependent regulation of *dlk-1* and *cebp-1* may function to protect cilia integrity.

To further explore this idea, we examined another cilia degeneration paradigm using *che-10* mutants. CHE-10/Rootletin anchors the transition zone of cilia at the basal body (13, 14). In *che-10(0)* animals, most amphid neurons form normal cilia and

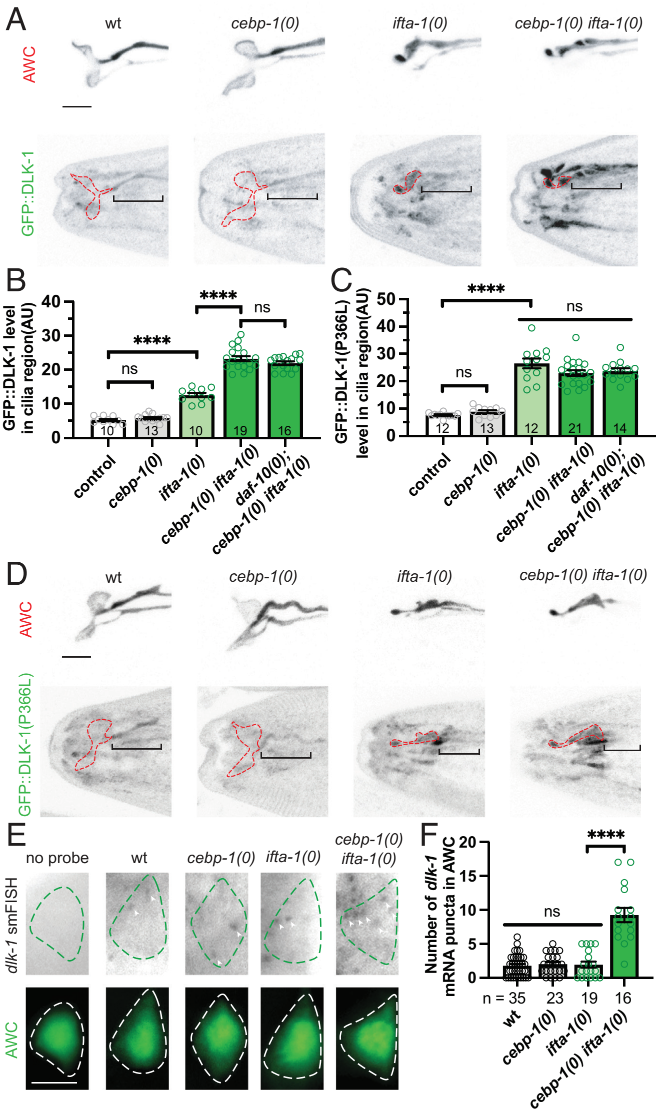

Fig. 5. CEBP-1 represses *dlk-1* transcription in AWC of *ift* mutants. (*A*) Shown as confocal Z-stack images of GFP::DLK-1 in AWC cilia and distal dendrites (labeled by *Podr-1-RFP*) in L4 animals of indicated genotypes. Red dashes outline AWC cilia and brackets indicate distal dendrites. Null *(0)* alleles used are *ifta-1(ju1644)* and *cebp-1(tm2807).* (Scale bar: 5 µm.) (*B* and *C*) Quantification of GFP::DLK-1 (*B*) and GFP::DLK-1(P366L) (*C*) fluorescence intensity in the cilia region in L4 animals of indicated genotypes. Data are represented as mean ± SEM, with each circle representing an individual animal and total numbers of animals analyzed shown in the columns. Statistics: Welch's ANOVA test with multiple comparison, corrected with the FDR method of Benjamini and Hochberg. ns, $P > 0.05$. ****=$P < 0.0001$. (*D*) Shown as confocal Z-stack images of GFP::DLK-1(P366L) in AWC cilia and distal dendrites (labeled by *Podr-1-RFP*) in L4 animals of indicated genotypes. Labels and alleles are same as in (*A*) (Scale bar: 5 µm.) (*E*) Shown are compound microscope images of single-molecule fluorescence in situ hybridization (smFISH) of *dlk-1* mRNA in AWC cell body in L4 animals of indicated genotypes. Top images show *dlk-1* mRNA puncta (white arrowheads) in AWC neuronal soma. Bottom images show AWC neuronal soma labeled by *Pstr-2-GFP*. ROIs are drawn in dashed lines. (Scale bar: 5 µm.) (*F*) Quantification of *dlk-1* smFISH in AWC cell body in L4 animals of indicated genotypes. Data are represented as mean ± SEM, with each circle representing an individual animal and total number of animals analyzed shown below the columns. Statistics: Welch's ANOVA test with multiple comparison, corrected with the FDR method of Benjamini and Hochberg. ns, $P > 0.05$. ****=$P < 0.0001$.

exhibit normal IFT at L1 stage; as larvae grow older, IFT diminishes, and cilia of several amphid neurons degenerate progressively (13). In our genetic screen, we identified two loss-of-function mutations in *che-10* showing increased GFP::DLK-1 similar to *ifta-1(0)* (*SI Appendix*, Table S2). We made *che-10(0); ifta-1(0)* double mutants and observed GFP::DLK-1 accumulation in the cilia region resembling each single mutants, consistent with them acting in the same pathway in regulating DLK-1.

To test whether IFT-dependent regulation of DLK-1 and CEBP-1 played a role in cilia degeneration in *che-10(0)*, we first assessed whether AWC cilia degenerate in *che-10(0)* mutants, as it was not previously reported. In L1 larvae of *che-10(0)*, AWC cilia showed normal fan-shaped morphology as in wild type. By L2 stage, ~30% of AWC showed noticeably reduced cilia with thinned connections between the cilia and the distal dendrites (*SI Appendix*, Fig. S6*A*). As animals grew to L4 and adults, the incidence of defective AWC cilia was increased to 40% and 60%, respectively (Fig. 6*A*). Similar morphological changes on AWB cilia in *che-10(0)* were also observed, albeit with a faster time course (*SI Appendix*, Fig. S6 *B* and *C*). We then assessed how the extent of AWC/AWB cilia degeneration in *che-10(0)* animals correlated with GFP::DLK-1 accumulation and CEBP-1::GFP expression. In wild-type AWC and AWB, which have morphologically normal cilia, GFP::DLK-1 was barely detectable at any developmental stages examined (Fig. 6*B* and *SI Appendix*, Fig. S7*A*). In *che-10(0)* animals showing AWC/AWB cilia degeneration, increased GFP::DLK-1 accumulation was observed in the distal dendrites and the remaining cilia (Fig. 6 *C* and *D* and *SI Appendix*, Fig. S7 *B* and *C*). CEBP-1::GFP intensity was also visibly increased in the nuclei of AWC and AWB of *che-10(0)* animals. In L1 and L2 of *che-10(0)*, AWC had low CEBP-1::GFP expression, based on the fluorescence intensity comparison to that in the neighboring non-neuronal cells, and showed increased CEBP-1::GFP in 50% of L3s, 65% of L4s and 90% of 1 day-old (1d) adults (Fig. 6 *E* and *F*). Similarly, AWB neurons of *che-10(0)* showed elevated CEBP-1::GFP in about 50% at L2 and 80% at L4 and 1d adults (*SI Appendix*, Fig. S7*D*), correlating with the more rapid course of AWB cilia degeneration. Additionally, loss of *cebp-1* enhanced GFP::DLK-1 accumulation in AWC and AWB in *che-10(0)* (*SI Appendix*, Fig. S7*E*), consistent with CEBP-1-mediated repression on *dlk-1* transcription. These data show that increased expression and activation of DLK-1 and CEBP-1 signaling correlate with AWC/AWB cilia degeneration in *che-10* mutants.

DLK-1 Attenuates AWC Cilia Degeneration Cell Autonomously.

We then asked how DLK-1 to CEBP-1 signaling affected *che-10(0)*-induced cilia degeneration. We scored AWC cilia morphology in *dlk-1(0); che-10(0)* and *che-10(0); cebp-1(0)* at each developmental stage. In L2 animals of *dlk-1(0); che-10(0)* and *che-10(0); cebp-1(0)*, 30% AWC showed cilia defects, similar to *che-10(0)* animals. The percentage of defective AWC cilia in both double mutants increased to about 60% at L3, and 80% at L4 and 1d adults, significantly higher than that in *che-10(0)* alone (Fig. 6*A*). Loss of *cebp-1* showed mild effects on *che-10(0)*-induced AWB cilia degeneration, possibly due to that AWB cilia degenerated much faster than AWC cilia (*SI Appendix*, Fig. S6*C*). The enhanced AWC cilia degeneration in *che-10(0); cebp-1(0)* at L4 and young adults was rescued by CEBP-1::GFP(*wgIs563*) (Fig. 6*A*). We also transgenically expressed wild-type *dlk-1* cDNA in AWC using the *Pstr-2* promoter. Seventy percent AWC in L4 *che-10(0)* single mutants showed cilia degeneration, compared to 90% in *dlk-1(0); che-10(0)* or in *che-10(0); cebp-1(0)*. *Pstr-2-dlk-1* expression did not change the percentage of AWC cilia degeneration in *che-10(0)* but reduced AWC cilia degeneration in *dlk-1(0); che-10(0)* to about 65%, comparable to that in *che-10(0)*. Moreover, the rescue effect of *Pstr-2-dlk-1* was blocked by *cebp-1(0)* (Fig. 6*G*). Together, our results show that DLK-1 acts

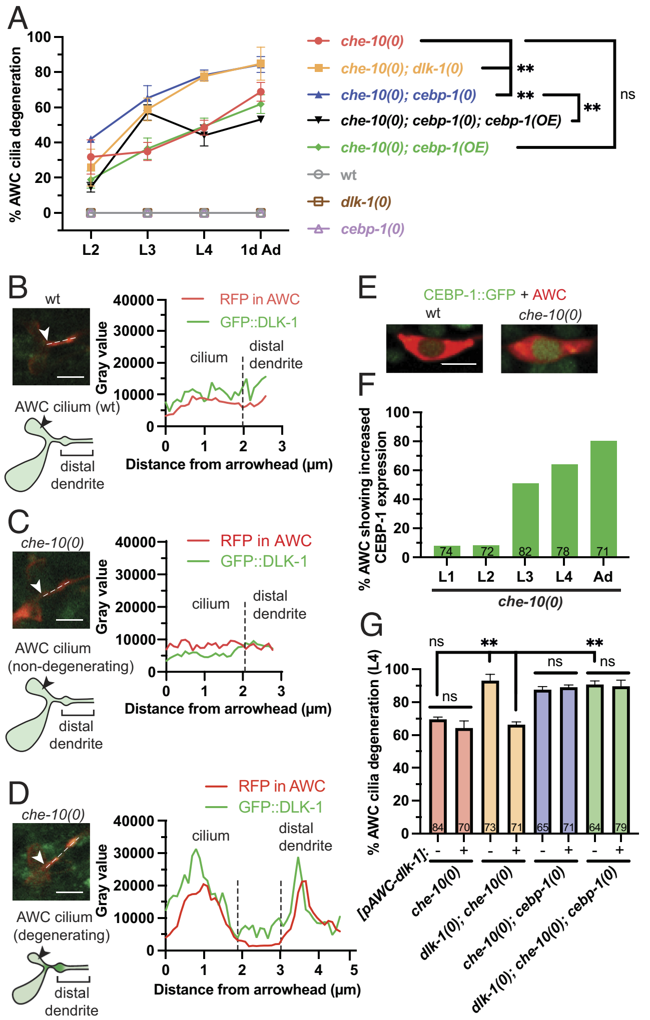

Fig. 6. DLK-1 and CEBP-1 attenuate AWC cilia degeneration in *che-10(0)* mutants. (*A*) Quantification of AWC cilia degeneration. Animals of indicated genotypes at L2, L3, L4 and day 1 adult (1dAd) were analyzed. Null *(0)* alleles used are *che-10(ju1752), dlk-1(km12), cebp-1(tm2807);* and *cebp-1(OE)* refers to CEBP-1::GFP*(wgIs563).* Data are represented as mean ± SEM. >70 total number of animals per genotype per stage were analyzed from three to five independent observations on different days. Statistics: Welch's ANOVA test with multiple comparison among *che-10(0)* and each of the other genotypes at L4 stage, corrected with the FDR method of Benjamini and Hochberg. ns, $P > 0.05$. **=0.01 > P > 0.001 (*B–D*) Plot profile analysis of GFP::DLK-1 at the cilia base of AWC marked by *Podr-1-RFP(oyIs44)* in wild-type (*B*), *che-10(0)* animals at nondegenerating state (*C*) and at degenerating state (*D*). Left panels are confocal images of AWC, along with illustration. Line profiles correspond to the dashed lines in AWC images. Cilia and distal dendrites are indicated by the peaks of RFP signal. (Scale bar: 5 µm.) (*E*) Confocal images of CEBP-1::GFP*(wgIs563)* in AWC (labeled by *Podr-1-RFP*) from wild-type and *che-10(0)* animals. (Scale bar: 5 µm.) (*F*) Quantification of the percentage of AWCs that show elevated CEBP-1::GFP*(wgIs563)* in *che-10(0); cebp-1(0)* at different stages. Numbers of animals analyzed are shown in each column. (*G*) Quantification of the percentage of AWC cilia showing degeneration in L4 animals of indicated genotypes. The strains containing the transgene *Pstr-2-dlk-1(juEx8262)* are marked with "+" and the ones with no transgene are marked with "–". Data are represented as mean ± SEM. Total numbers of animals analyzed are shown in each column. Statistics: Welch's ANOVA test with multiple comparison, corrected with the FDR method of Benjamini and Hochberg. ns, $P > 0.05$. **=0.01 > P > 0.001.

cell autonomously through CEBP-1 to protect AWC cilia from *che-10(0)*-induced degeneration.

Discussion

Neurons exhibit exquisitely compartmentalized actions and utilize a variety of mechanisms to regulate local protein composition and dynamics. Even the same molecule may be differentially regulated depending on subcellular localization. DLK proteins have been extensively studied for their roles in axonal and synapse compartments, where increasing their expression triggers activation of the downstream signal transduction in a context-specific manner (20). In this study, through unbiased genetic screening for factors constraining expression levels of *C. elegans* DLK-1, we uncovered a tight regulation on DLK-1 in sensory neurons (Fig. 7). The DLK-1 signaling in the ciliated sensory neurons diverges from those operating in axonal and synapse compartments and also shows a high degree of context specificity.

Intraflagellar transport plays essential roles to deliver cilia cargoes and balance cilia proteome. Disruption of any components involved in intraflagellar transport leads to a general alteration of cilia morphology (15, 55). While the low basal expression level of DLK-1 restrains our ability to detect its trafficking, we show that the increased DLK-1 accumulation in the sensory endings in *ift* mutants is unlikely a secondary effect of reduced cilia length or nonspecific alteration of cilia proteome. DLK-1 expression is unaltered in mutants of *oig-8* or *tbb-4,* which change cilia morphology but not IFT. DLK-1 expression is increased in *dyf-5* mutants, in which cilia grow more or ectopically. Importantly, in response to acute IFT disruption, active DLK-1 accumulates rapidly and reversibly, before detectable changes in the cilia morphology and localization of IFT particles. A previous study reported that movement of several IFT components is significantly reduced in *dlk-1(0)* mutants (33). These observations argue for an active interaction between DLK-1 and IFT. Moreover, local accumulation of DLK-1 following IFT disruption causes activation of

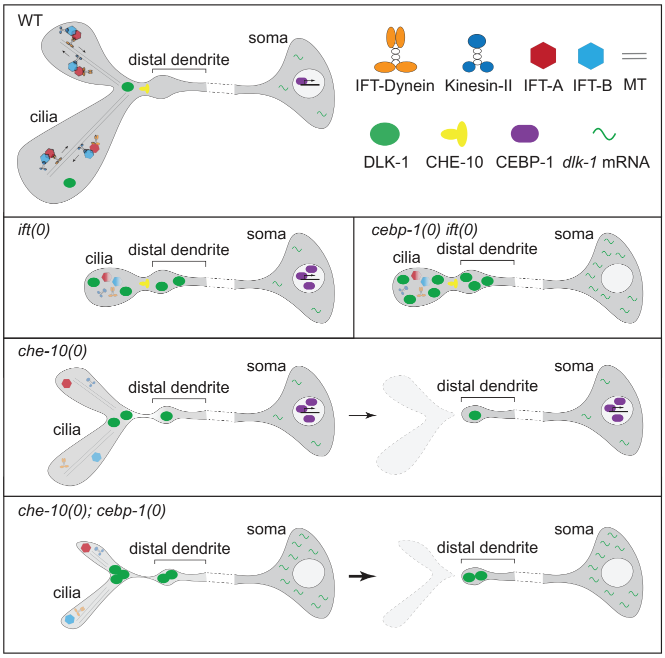

Fig. 7. Summary of the interaction of IFT, CHE-10, DLK-1 and CEBP-1 in AWC neuron. In wild-type (WT) AWC neurons, DLK-1 is present at very low level in the cilium and distal dendrite, and CEBP-1 has basal level of expression in the nucleus. In *ift(0)* mutants, AWC cilia wing is reduced to a knob, DLK-1 accumulates in the remaining cilium and distal dendrite, and CEBP-1 expression is elevated. In *cebp-1(0) ift(0)* double mutants, cilia morphology and IFT transport remain defective as in *ift(0), dlk-1* mRNA is increased, leading to further increased DLK-1 accumulation in cilia stump and distal dendrite. In *che-10(0)* animals, AWC cilia show progressive degeneration as larvae grow (~60% in L4), DLK-1 accumulates in degenerating cilia and distal dendrites, accompanied with increased CEBP-1 in nuclei. *che-10(0); cebp-1(0)* animals show enhanced AWC cilia degeneration (~80% in L4) and increased DLK-1 accumulation, compared to *che-10(0)* single mutant.

DLK-1 and its downstream signaling, which then imposes a negative feedback via CEBP-1 to restrain DLK-1 levels in cilia. DLK-1 may be dynamically associated with IFT or other cilia components; however, we do not know how DLK-1 detects changes in IFT. We speculate that the active interaction between IFT and DLK-1 provides a surveillance to modulate trafficking state in cilia.

Both DLK-1 and its known downstream factor CEBP-1 are expressed in many ciliated sensory neurons. Both proteins are normally kept at low levels and increased in abundance upon IFT disruption. Yet, their relationship varies among the ciliated neuron types and also differs from that operating in axons and synapses of other neuron types. In AWB and AWC neurons, which have elaborate cilia morphology, upregulation of CEBP-1 follows the increased accumulation of DLK-1 and is dependent on DLK-1, consistent with their known relationship in axons and synapses. Unexpectedly, under IFT disruption, elevated CEBP-1 represses *dlk-1* transcription to dampen further elevation of DLK-1. In ASH and ASI neurons, which have simple rod-shaped cilia morphology, upregulation of CEBP-1 is largely independent of DLK-1, which is also in contrast to their relationship in synapse formation regulated by *rpm-1* (56), and this study). Two published studies revealed different contexts involving DLK-1 signaling in the rod-cilia sensory neurons. One showed that DLK-1 and its downstream kinases mediate shortening of rod-cilia induced by constitutive activation of a ciliary G protein α subunit (33). Another showed that DLK-1 regulates the stability of the photoreceptor LITE-1 in the ASH polymodal neurons, albeit independent of cilia (34). Both studies place endocytosis downstream of DLK-1, although it remains unknown whether such effects involve CEBP-1. Furthermore, the IFT-induced, DLK-1-independent, regulation of CEBP-1 in many ciliated neurons raises open questions in our understanding of neuron-type and context-specific signaling. It has been reported that PMK-3, the key MAP kinase downstream of DLK-1 in synapse formation and axon regeneration (23), can function independently of DLK-1 in BAG neurons (57). CEBP-1 is also known to function independent of DLK-1 in other cellular contexts (58, 59). Future work is required to tease apart the regulatory elements that mediate cell-type specificity of CEBP-1 expression. The observation that upregulation of CEBP-1 follows DLK-1 accumulation in cilia also suggests that local protein activity state in cilia triggers long-distance retrograde signaling to nuclei. A recent study has reported that altering the ciliary MAK kinase DYF-5 triggers nuclear RNA editing (60). These findings raise interesting future questions to dissect the communication mechanisms between neuronal compartments.

Cilia play important roles not only in sensory processing but also in the health of cells and organisms. Multiple genes and pathways work together to ensure the formation and maintenance of morphologically and functionally diverse cilia (2). While loss or overexpression of DLK-1 or CEBP-1 does not alter cilia development or maintenance, in animals undergoing cilia degeneration due to the loss of Rootletin/CHE-10, removing *dlk-1* or *cebp-1* accelerates cilia degeneration, supporting a neuroprotective role of this IFT-dependent regulatory loop. CHE-10 orchestrates IFT assembly and cilia anchoring at the basal bodies, likely via interaction with additional proteins besides IFT core components. We speculate that in degenerating cilia of *che-10* mutants, DLK-1 signaling both senses IFT disruption and promotes interaction of the proteins residing in the cilia base to engage neuroprotection. The moderate neuroprotective effects of DLK-1 and CEBP-1 imply multilayered functional redundancy among ciliary protective molecules. Dysfunction of cilia leads to a broad spectrum of human diseases called ciliopathy (2). Teasing apart the specificity of the redundant signaling network in cilia remains an important goal in the search for effective treatment of pathological conditions.

Limitation of the Study

We intended to investigate the regulation of endogenous DLK-1 using knock-in fluorescent protein tagging. However, the low visibility of fluorescence is prohibitive to resolve the spatial relationship of DLK-1 with other ciliary proteins. We attempted to boost the fluorescence signals using the split-GFP intersection approach but were unable to recapitulate DLK-1 localization in cilia. Our data show that DLK-1 abundance in the sensory endings is regulated by IFT, but our analysis does not identify the underlying mechanism. Another unexpected, but interesting, finding is that CEBP-1 expression in sensory neurons is also under tight control of IFT, but only partly dependent on DLK-1. Despite the tight regulation on protein expression, the functional impact of the DLK-1 and CEBP-1 signaling appears to be modest. Sensory cilia constantly detect environmental stimuli and help organisms to initiate precise response. It is possible that to buffer unexpected or harsh conditions cilia need redundant mechanisms to tightly control cellular signaling components.

Materials and Methods

***C. elegans* Genetics and Transgenesis.** *C. elegans* wild type was the N2 Bristol strain. Strains were maintained on Nematode Growth Media plates seeded with *E. coli* OP50 at 20 °C, unless stated otherwise. All experiments were performed with hermaphrodites, and males were used only for crosses. Compound mutants were generated using standard procedures (61). The strain information is in *SI Appendix*, Table S1. Mutant alleles were confirmed by PCR or Sanger sequencing as described in *SI Appendix*, Table S2. Transgenic animals were generated following standard procedures (62); and expression constructs were made using the Gateway cloning system (Invitrogen) and Gibson Assembly (NEB), as described in *SI Appendix*, *Supplemental Methods*.

CRISPR-Cas9 Genome Editing to Generate *GFP::dlk-1(ju1579)*. We generated the *GFP::dlk-1(ju1579)* knock-in allele following the CRISPR-Cas9 genome engineering method with a self-excising drug selection cassette (SEC) as described (63). Using the CRISPR design tool (http://crispr.mit.edu), we selected sgRNA for the target sequence 5′-TAAAATGACATCTACCACAA**TGG**-3′, with the PAM site TGG mutated to TGT, which caused DLK-1(V7L). sgRNA was inserted into pDD162 vector (Addgene #47549) to generate pCZGY3280. We amplified 1.2 kb homology arms on either side of target sequence and inserted the amplicon to pDD282 (Addgene #66823, FP::SEC vector) to generate pCZGY3279. We injected N2 hermaphrodites with a DNA mix containing pCZGY3280 (50 ng/μL) and pCZGY3279 (10 ng/μL), coinjection marker pGH8 (Prab-3::mCherry; Addgene #19359, 10 ng/μL), pCFJ104 (Pmyo-3::mCherry; Addgene #19328, 5 ng/μL), and pCFJ90 (Pmyo-2::mCherry; Addgene #19327, 2.5 ng/μL). *GFP-SEC-dlk-1(ju1578)* knock-in animals were selected based on rollers without red coinjection markers following hygromycin treatment and were subjected to heat shock at 34 °C for 4 h to remove SEC. We confirmed *GFP::dlk-1(ju1579)* genomic sequence by Sanger sequencing and verified in mRNA products that GFP was in-frame to the second amino acid Threonine of DLK-1.

Isolation of *ift* Mutants and WGS Analysis. The genetic screen using *dlk-1(ju1579)* will be described in full elsewhere. Briefly, we carried out mutagenesis using 50 mM ethyl methanesulfonate on CZ26350 *GFP::dlk-1(ju1579); rpm-1(ju44); cebp-1(tm2807)*. F2 progeny were screened by visual inspection of altered GFP::DLK-1 expression using compound fluorescence microscopy. Multiple independent mutants showed increased GFP::DLK-1 at the tip of the head; we performed WGS analysis for subsets of these mutants. Additional analysis of these mutants and verification of *ift* mutants are described in *SI Appendix*, *Supplemental Methods*.

Single-Molecule Fluorescence In Situ Hybridization. We performed smFISH on L4-stage animals according to a modified Stellaris protocol, as detailed in *SI Appendix*, *Supplemental Methods*.

Confocal Fluorescence Microscopy. Animals were anesthetized in 1 mM levamisole on 10% agarose pads and imaged using a 63× oil immersion objective on a Zeiss LSM800 confocal microscope. Laser settings were adjusted for each fluorescence marker described in details in *SI Appendix*, *Supplemental Methods*.

Statistical Analysis. Statistical analysis was performed using GraphPad Prism 8 (GraphPad Software, Inc.). Statistical significance was determined using Fisher's exact test, Welch's ANOVA test for multiple comparison corrected with the false discovery rate (FDR) method of Benjamini and Hochberg, or Dunn's multiple comparison test as appropriate. $P > 0.05$ was considered not significant (ns). $P < 0.05$ (*); $P < 0.01$ (**); $P < 0.001$ (***); and $P < 0.0001$ (****) were considered significant differences. Data are represented as mean ± SEM. The numbers of individual samples are shown in or below columns in corresponding figures.

Data, Materials, and Software Availability. All study data are included in the article and/or *SI Appendix*.

ACKNOWLEDGMENTS. We greatly appreciate discussions with P. Sengupta and her lab members, as well as A.D. Chisholm, G. Ou, and C.-Y. Su for comments on the manuscript. We thank P. Sengupta, M. Leroux, G. Ou, and A. Desai for strains and expression constructs, V. Lazetic and E. Troemel for advice on smFISH experiments, Z. Wu for assistance in laser axotomy, and B. Xie for participation in the genetic screen. We thank members of the Jin and Chisholm laboratories for valuable inputs and support throughout the work. Some strains were obtained from *Caenorhabditis* Genetics Center, which is funded by the NIH Office of Research Infrastructure Programs P40 OD010440. Y.S. received an Innovative Research Grant (#2020-1711) from the Kavli Institute of Brain and Mind at the University of California San Diego. This work was supported by grants from NIH to Y.J. (R37 NS035546 and R35 NS127314).

1. Z. Anvarian, K. Mykytyn, S. Mukhopadhyay, L. B. Pedersen, S. T. Christensen, Cellular signalling by primary cilia in development, organ function and disease. *Nat. Rev. Nephrol.* **15**, 199–219 (2019).
2. J. F. Reiter, M. R. Leroux, Genes and molecular pathways underpinning ciliopathies. *Nat. Rev. Mol. Cell Biol.* **18**, 533–547 (2017).
3. H. Ishikawa, W. F. Marshall, Ciliogenesis: Building the cell's antenna. *Nat. Rev. Mol. Cell Biol.* **12**, 222–234 (2011).
4. G. Ou, J. M. Scholey, Motor cooperation during mitosis and ciliogenesis. *Annu. Rev. Cell Dev. Biol.* **38**, 49–74 (2022).
5. J. L. Rosenbaum, G. B. Witman, Intraflagellar transport. *Nat. Rev. Mol. Cell Biol.* **3**, 813–825 (2002).
6. H. Ishikawa, W. F. Marshall, Intraflagellar transport and ciliary dynamics. *Cold Spring Harb. Perspect. Biol.* **9**, a021998 (2017).
7. K. Nakayama, Y. Katoh, Architecture of the IFT ciliary trafficking machinery and interplay between its components. *Crit. Rev. Biochem. Mol. Biol.* **55**, 179–196 (2020).
8. M. Taschner, E. Lorentzen, The intraflagellar transport machinery. *Cold Spring Harb. Perspect. Biol.* **8**, a028092 (2016).
9. M. A. Silverman, M. R. Leroux, Intraflagellar transport and the generation of dynamic, structurally and functionally diverse cilia. *Trends Cell Biol.* **19**, 306–316 (2009).
10. P. N. Inglis, G. Ou, M. R. Leroux, J. M. Scholey, The sensory cilia of *Caenorhabditis elegans*. *WormBook* **2007**, 1–22 (2007).
11. P. Phirke *et al.*, Transcriptional profiling of *C. elegans* DAF-19 uncovers a ciliary base-associated protein and a CDK/CCRK/LF2p-related kinase required for intraflagellar transport. *Dev. Biol.* **357**, 235–247 (2011).
12. P. Swoboda, H. T. Adler, J. H. Thomas, The RFX-type transcription factor DAF-19 regulates sensory neuron cilium formation in *C. elegans*. *Mol. Cell* **5**, 411–421 (2000).
13. S. Mohan, T. A. Timbers, J. Kennedy, O. E. Blacque, M. R. Leroux, Striated Rootlet and Nonfilamentous Forms of Rootletin Maintain Ciliary Function. *Curr. Biol*. **23**, 2016–2022 (2013).
14. J. Yang *et al.*, Rootletin, a novel coiled-coil protein, is a structural component of the ciliary rootlet. *J. Cell Biol.* **159**, 431–440 (2002).
15. S. Mukhopadhyay *et al.*, Distinct IFT mechanisms contribute to the generation of ciliary structural diversity in *C. elegans*. *EMBO J.* **26**, 2966–2980 (2007).
16. J. Burghoorn *et al.*, Mutation of the MAP kinase DYF-5 affects docking and undocking of kinesin-2 motors and reduces their speed in the cilia of *Caenorhabditis elegans*. *Proc. Natl. Acad. Sci. U.S.A.* **104**, 7157–7162 (2007).
17. X. Jiang *et al.*, DYF-5/MAK–dependent phosphorylation promotes ciliary tubulin unloading. *Proc. Natl. Acad. Sci. U.S.A.* **119**, e2207134119 (2022).
18. A. K. Maurya, T. Rogers, P. Sengupta, A CCRK and a MAK kinase modulate cilia branching and length via regulation of axonemal microtubule dynamics in *Caenorhabditis elegans*. *Curr. Biol.* **29**, 1286–1300.e4 (2019).
19. K. Howell, O. Hobert, Morphological Diversity of *C. elegans* Sensory Cilia Instructed by the Differential Expression of an Immunoglobulin Domain Protein. *Curr. Biol*. **27**, 1782–1790.e5 (2017).
20. Y. Jin, B. Zheng, Multitasking: Dual leucine zipper-bearing kinases in neuronal development and stress management. *Annu. Rev. Cell Dev. Biol.* **35**, 501–521 (2019).
21. C. A. Collins, Y. P. Wairkar, S. L. Johnson, A. DiAntonio, Highwire restrains synaptic growth by attenuating a MAP kinase signal. *Neuron* **51**, 57–69 (2006).
22. J. W. Lewcock, N. Genoud, K. Lettieri, S. L. Pfaff, The ubiquitin ligase Phr1 regulates axon outgrowth through modulation of microtubule dynamics. *Neuron* **56**, 604–620 (2007).
23. K. Nakata *et al.*, Regulation of a DLK-1 and p38 MAP kinase pathway by the ubiquitin ligase RPM-1 is required for presynaptic development. *Cell* **120**, 407–420 (2005).
24. A. Daviau *et al.*, Down-regulation of the mixed-lineage dual leucine zipper-bearing kinase by heat shock protein 70 and its co-chaperone CHIP. *J. Biol. Chem.* **281**, 31467–31477 (2006).
25. S. Karney-Grobe, A. Russo, E. Frey, J. Milbrandt, A. DiAntonio, HSP90 is a chaperone for DLK and is required for axon injury signaling. *Proc. Natl. Acad. Sci. U.S.A.* **115**, E9899–E9908 (2018).
26. C. Zheng *et al.*, Opposing effects of an F-box protein and the HSP90 chaperone network on microtubule stability and neurite growth in *Caenorhabditis elegans*. *Development* **147**, dev189886. (2020).
27. S. M. Holland *et al.*, Palmitoylation controls DLK localization, interactions and activity to ensure effective axonal injury signaling. *Proc. Natl. Acad. Sci. U.S.A.* **113**, 763–768 (2016).
28. J. Niu *et al.*, Coupled control of distal axon integrity and somal responses to axonal damage by the palmitoyl acyltransferase ZDHHC17. *Cell Rep.* **33**, 108365 (2020).
29. A. Ghosh-Roy, Z. Wu, A. Goncharov, Y. Jin, A. D. Chisholm, Calcium and cyclic AMP promote axonal regeneration in *Caenorhabditis elegans* and require DLK-1 kinase. *J. Neurosci.* **30**, 3175–3183 (2010).
30. Y. Hao *et al.*, An evolutionarily conserved mechanism for cAMP elicited axonal regeneration involves direct activation of the dual leucine zipper kinase DLK. *eLife* **5**, e14048 (2016).
31. D. Yan, Y. Jin, Regulation of DLK-1 kinase activity by calcium-mediated dissociation from an inhibitory isoform. *Neuron* **76**, 534–548 (2012).
32. C. D. Pozniak *et al.*, Dual leucine zipper kinase is required for excitotoxicity-induced neuronal degeneration. *J. Exp. Med.* **210**, 2553–2567 (2013).
33. A. van der Vaart, S. Rademakers, G. Jansen, DLK-1/p38 MAP Kinase signaling controls cilium length by regulating RAB-5 mediated endocytosis in *Caenorhabditis elegans*. *PLOS Genet.* **11**, e1005733 (2015).
34. X. Zhang *et al.*, A cilia-independent function of BBSome mediated by DLK-MAPK signaling in *C. elegans* photosensation. *Dev. Cell* **57**, 1545–1557.e4 (2022).
35. A. B. Byrne *et al.*, Insulin/IGF1 signaling inhibits age-dependent axon regeneration. *Neuron* **81**, 561–573 (2014).
36. M. Hammarlund, P. Nix, L. Hauth, E. M. Jorgensen, M. Bastiani, Axon regeneration requires a conserved MAP kinase pathway. *Science* **323**, 802–806 (2009).
37. D. Yan, Z. Wu, A. D. Chisholm, Y. Jin, The DLK-1 kinase promotes mRNA stability and local translation in *C. elegans* synapses and axon regeneration. *Cell* **138**, 1005–1018 (2009).
38. D. K. Cheerambathur *et al.*, The kinetochore-microtubule coupling machinery is repurposed in sensory nervous system morphogenesis. *Dev. Cell* **48**, 864–872.e7 (2019).
39. L. R. Bell, S. Stone, J. Yochem, J. E. Shaw, R. K. Herman, The molecular identities of the *Caenorhabditis elegans* intraflagellar transport genes dyf-6, daf-10 and osm-1. *Genetics* **173**, 1275–1286 (2006).
40. O. E. Blacque *et al.*, The WD repeat-containing protein IFTA-1 is required for retrograde intraflagellar transport. *Mol. Biol. Cell* **17**, 5053–5062 (2006).
41. S. R. Wicks, C. J. de Vries, H. G. A. M. van Luenen, R. H. A. Plasterk, CHE-3, a cytosolic dynein heavy chain, is required for sensory cilia structure and function in *Caenorhabditis elegans*. *Dev. Biol.* **221**, 295–307 (2000).
42. M. Taipale *et al.*, Quantitative analysis of Hsp90-client interactions reveals principles of substrate recognition. *Cell* **150**, 987–1001 (2012).
43. J. Collet, C. A. Spike, E. A. Lundquist, J. E. Shaw, R. K. Herman, Analysis of *osm-6*, a gene that affects sensory cilium structure and sensory neuron function in *Caenorhabditis elegans*. *Genetics* **148**, 187–200 (1998).
44. E. Tortosa *et al.*, Stress-induced vesicular assemblies of dual leucine zipper kinase are signaling hubs involved in kinase activation and neurodegeneration. *EMBO J.* **41**, e110155 (2022).
45. X. Xiong *et al.*, Protein turnover of the Wallenda/DLK kinase regulates a retrograde response to axonal injury. *J. Cell Biol.* **191**, 211–223 (2010).
46. P. Yi, W.-J. Li, M.-Q. Dong, G. Ou, Dynein-Driven Retrograde Intraflagellar Transport Is Triphasic in *C. elegans* Sensory Cilia. *Curr. Biol.* **27**, 1448–1461.e7 (2017).
47. J. C. Schafer, C. J. Haycraft, J. H. Thomas, B. K. Yoder, P. Swoboda, XBX-1 encodes a dynein light intermediate chain required for retrograde intraflagellar transport and cilia assembly in *Caenorhabditis elegans*. *Mol. Biol. Cell* **14**, 2057–2070 (2003).
48. A. Lanjuin, M. K. VanHoven, C. I. Bargmann, J. K. Thompson, P. Sengupta, Otx/otd homeobox genes specify distinct sensory neuron identities in *C. elegans*. *Dev. Cell* **5**, 621–633 (2003).
49. L. Hao *et al.*, Intraflagellar transport delivers tubulin isotypes to sensory cilium middle and distal segments. *Nat. Cell Biol.* **13**, 790–798 (2011).
50. D. D. Hurd, R. M. Miller, L. Núñez, D. S. Portman, Specific α- and β-tubulin isotypes optimize the functions of sensory cilia in *Caenorhabditis elegans*. *Genetics* **185**, 883–896 (2010).
51. V. L. Jensen *et al.*, Role for intraflagellar transport in building a functional transition zone. *EMBO Rep.* **19**, e45862 (2018).
52. A. Bounoutas *et al.*, Microtubule depolymerization in *Caenorhabditis elegans* touch receptor neurons reduces gene expression through a p38 MAPK pathway. *Proc. Natl. Acad. Sci. U.S.A.* **108**, 3982–3987 (2011).
53. A. Raj, P. van den Bogaard, S. A. Rifkin, A. van Oudenaarden, S. Tyagi, Imaging individual mRNA molecules using multiple singly labeled probes. *Nat. Methods* **5**, 877–879 (2008).
54. E. R. Troemel, A. Sagasti, C. I. Bargmann, Lateral Signaling Mediated by Axon Contact and Calcium Entry Regulates Asymmetric Odorant Receptor Expression in *C. elegans*. *Cell* **99**, 387–398 (1999).
55. K. F. Lechtreck, IFT–cargo interactions and protein transport in cilia. *Trends Biochem. Sci.* **40**, 765–778 (2015).

56. J. G. Crump, M. Zhen, Y. Jin, C. I. Bargmann, The SAD-1 kinase regulates presynaptic vesicle clustering and axon termination. *Neuron* **29**, 115–129 (2001).
57. L. B. Horowitz, J. P. Brandt, N. Ringstad, Repression of an activity-dependent autocrine insulin signal is required for sensory neuron development in *C. elegans*. *Development* **146**, dev.182873 (2019).
58. K. W. Kim *et al.*, Coordinated inhibition of C/EBP by Tribbles in multiple tissues is essential for *Caenorhabditis elegans* development. *BMC Biol.* **14**, 104 (2016).
59. D. L. McEwan *et al.*, Tribbles ortholog NIPI-3 and bZIP transcription factor CEBP-1 regulate a *Caenorhabditis elegans* intestinal immune surveillance pathway. *BMC Biol.* **14**, 105 (2016).
60. D. Li *et al.*, RNA editing restricts hyperactive ciliary kinases. *Science* **373**, 984–991 (2021).
61. S. Brenner, The genetics of *Caenorhabditis elegans*. *Genetics* **77**, 71–94 (1974).
62. C. C. Mello, J. M. Kramer, D. Stinchcomb, V. Ambros, Efficient gene transfer in *C. elegans*: Extrachromosomal maintenance and integration of transforming sequences. *EMBO J.* **10**, 3959–3970 (1991).
63. D. J. Dickinson, A. M. Pani, J. K. Heppert, C. D. Higgins, B. Goldstein, Streamlined genome engineering with a self-excising drug selection cassette. *Genetics* **200**, 1035–1049 (2015).